Intrusions induce global warming before continental flood basalt volcanism

Xiaochuan Tian ✉ and W. Roger Buck

Extinction events are known to correlate with continental flood basalt eruptions. Massive carbon degassing from these eruptions can have catastrophic impacts on the global climate and biospheres. However, high-precision geochronology from the Deccan Traps and the Columbia River Basalt Group suggests that the onset of global warming precedes the main phase of flood basalt eruptions by several hundred thousand years. Here we construct a numerical model of sill intrusion to investigate this lag between warming and eruptions. The model determines the depth of sill intrusion depending on the evolving crustal density and temperature structures. Main-phase eruptions occur when the average density above the sill intrusion is greater than the magma density. When combined with a carbon-cycle simulation, the models can reproduce the observed timing and amplitude of the global warming events associated with the Deccan Traps and the Columbia River Basalt Group. We therefore conclude that major eruptions of continental flood basalts require densification of the crust by voluminous basaltic magma intrusions. The crystallization of such pre-eruption intrusions could release enough carbon dioxide to drive substantial global warming before the main phase of flood basalt volcanism.

Large igneous provinces (LIPs) represent Earth's most voluminous magmatic events. Major LIPs typically extrude more than 10^6 km³ of magma within one million years[1]. Estimates of carbon dioxide (CO_2) concentrations in primitive LIP magma vary from 0.1 to ~2 weight per cent (wt%) (ref. [2]), and thus extrusions of a LIP could release as much as 6×10^{16} kg of CO_2. Such fluxes are enough to substantially warm Earth's climate[3]. The emplacement of LIPs is widely recognized to be coeval with climate changes and mass extinctions events[4,5]. These temporal correlations support the idea that flood basalt eruptions that release massive amounts of greenhouse gases may cause climatic excursions and biotic crises.

New geochronological data for both the Deccan Traps and the Columbia River Basalt Group (CRBG) complicates the hypothetical causal link between LIP volcanism and global warming. For the Deccan Traps, one of the largest LIPs, new data suggest that more than 70% of the flood basalts[6–8] were emplaced ~300 kyr after the onset of an average 2 °C global warming[3] (Fig. 1a and Supplementary Fig. S1). For the CRBG, volcanic CO_2 release probably caused global warming and polar ice melting events during the Miocene Climate Optimum (MCO; 17–14.7 million years ago (Ma)) (ref. [9]). However, recent high-precision geochronology data[10] indicate that 95% of the CRBG erupted ~300 yr after the onset of the MCO[9,11] (Fig. 1b).

For continental LIPs, geophysical data indicate that ~10 times more magma is intruded as is extruded[1,12]. For example, beneath the Deccan Traps[13–19], CRBG[20–22], Emeishan[23], Siberian[24] and Etendeka[25] LIPs, seismic velocities, gravity and electrical anomalies indicate both vertically[26] and laterally[27] extensive mafic crustal intrusions. Geochemical studies also indicate that up to 85% of the total magma volume was intruded within the crust during the CRBG emplacement[28].

Crystallization releases nearly all the CO_2 dissolved in basaltic magma[29]. Gas released from solidifying intruded magma could traverse the overlying crust and add to the atmosphere through fractures, faults and hydrothermal vents[30], as inferred for Yellowstone[31], the East African Rift[32], the Central Atlantic Magmatic Province[33] and the Deccan Traps[34]. Thus, the intrusion and solidification of millions of cubic kilometres of basaltic LIP magma would release far more CO_2 than released by extrusion. The pattern of global warming preceding the LIP eruptions would be explained if the intrusion preceded the extrusion.

Crustal densification induces LIP main-phase eruptions

Geochemical studies indicate that mantle-derived magma resides for thousands of years in transcrustal magmatic systems before it extrudes[35]. For extrusion, the pressure in such magma reservoirs must be higher than the hydrostatic pressure at the base of a column of magma from the surface to the reservoirs. The long-term average pressure in a magma reservoir should equal the lithostatic pressure (the average density of the overlying crust times the acceleration of gravity and the depth below the surface). Magma reservoirs can be 'overpressured' relative to lithostatic pressure, but it is difficult to maintain overpressure if magma reservoirs are large and/or are surrounded by low viscosity crust[36,37]. For many LIPs, the crustal intrusions are thought to be very large, with lateral dimensions of up to hundreds of kilometres[20,27,38], so overpressures should be negligible[37]. Thus, large flood basalt extrusions may only happen when the average overburden density is greater than the magma density.

Particularly clear evidence for the importance of crustal density in controlling eruptions comes from plate-spreading centres. Constraints on the depth of axial magma chambers and the crustal density structure at oceanic spreading centres are superior to those for continental magma bodies due to the greater resolving power of marine seismic methods. Axial magma chambers are fairly small (~1 km wide) and are seen to lie at or below the depth at which the average overburden density equals the magma density, a depth that is termed the 'level of eruptibility'[39,40].

Continental crustal density generally increases with depth, as the upper crust is richer in less dense felsic rocks when compared with the more mafic lower crust. Seismic velocity measurement is one of the main ways to estimate crustal density at depth. Figure 2a shows the average seismic velocity with depth in continental crust based on 560 worldwide seismic experiments[41]. We infer the average
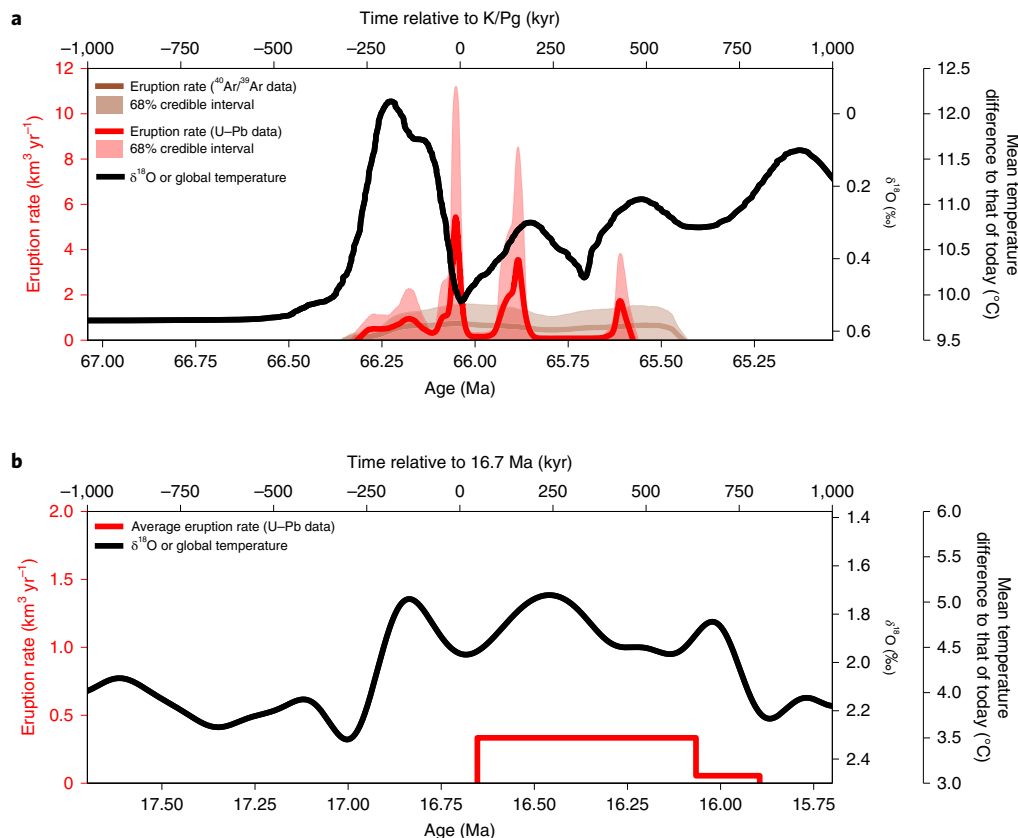
Lamont-Doherty Earth Observatory, Columbia University, Palisades, NY, USA. ✉e-mail: x.tian@columbia.edu

Fig. 1 | Global temperature variations within 1,000 kyr of the approximate onset of the main volcanic phases of the Deccan Traps[6,7] and CRBG[10] LIPs.
a,b, The Deccan Traps (**a**) and CRBG–MCO (**b**) Cretaceous–Palaeogene (K/Pg) global warming. The black lines are $\delta^{18}O$ data or estimated temperature variations with time[3,9,11]. For the Deccan Traps, the eruption rates with their corresponding 68% credible intervals are from ref. [50]. Details of the geochronology models and temperature estimates are described in the Supplementary Information. Note the different scales for the eruption rate in **a** and **b**.

crustal density structure following a standard relationship between seismic velocity and density for crustal rocks at different depths[41]. Assuming a typical basaltic magma density[42] of 2,800 kg m^{-3} and a crustal density structure shown in Fig. 2a, the lithostatic pressure would be enough to drive eruptions only if the magma is sourced from sills that are deeper than 27 km (Fig. 2b, red). For sills at shallower depths (Fig. 2b, blue), the magma should not reach the surface even with an open conduit to the surface.

As noted, seismic velocities beneath several LIPs[13–15,17,18,20–25] are markedly higher than that for a globally averaged continental crust[41]. Although constraining the depth range of high-velocity intrusives is difficult, several recent seismic, magnetotelluric and gravity experiments that span much of the Deccan Traps[13–19] or in the area of the main dyke swarms of the CRBG[20–22] show evidence for mafic intrusions in the mid-to-upper crust. One example profile is shown in Fig. 2c. Applying a standard velocity-to-density conversion[41], we found a denser than average middle and upper crust (Fig. 2c). Under this density structure, magma is eruptible from much shallower sills at a depth of ~15 km (Fig. 2d). The denser crust beneath the LIPs is probably due to basaltic crustal intrusions[13,14,16,18,19].

We suggest that a crustal densification due to voluminous magma intrusion and solidification is necessary for the extrusion of continental flood basalts. The massive magma flux for most LIPs is thought to originate in active upwellings or plumes of hotter-than-normal mantle[43]. Partial melting occurs as the mantle rises and pressure decreases. The short duration of LIP magmatic events indicates that the plume-induced melt flux increases and then decreases on a timescale shorter than a few million years. The

heat from the magma enables an intruded sill to heat the overlying crust and allows a rapid decrease in the intrusion depth during the phase of flux increase. As the melt flux wanes, the crust above a sill should cool and the sill intrusion depth deepen. Through this shallowing and deepening cycle, dense solidified mafic intrusions are emplaced into the crust, which shifts the level of eruptibility.

CO$_2$ released from intrusions induces pre-eruption global warming

Precise controls on sill-opening depths are controversial, but temperature structure is almost certain to be a critical factor. Temperature affects the strength of the rocks that must be deformed to allow opening. Temperature structure also controls the rate of cooling of magma in the sills. Both effects mean that the hotter the crust, the shallower the minimum depth of sill opening. Analytical relations between the heat released from intrusion and the steady-state temperature structure of the crust, described in Methods, show that reasonable magma flux variations can produce the kinds of changes in sill depth required to cause extrusion late in the emplacement of a LIP.

As the crustal thermal structure does not respond instantaneously to changes in magmatic heat input, we need a time-dependent model that includes diffusion and advection of heat as well as reasonable assumptions about the controls on sill depth. The key question to test is whether a reasonable model can produce a major phase of extrusion starting a few hundred thousand years after the onset of detectable global warming that is caused by the CO$_2$ degassed from the preceding crustal magma intrusions.
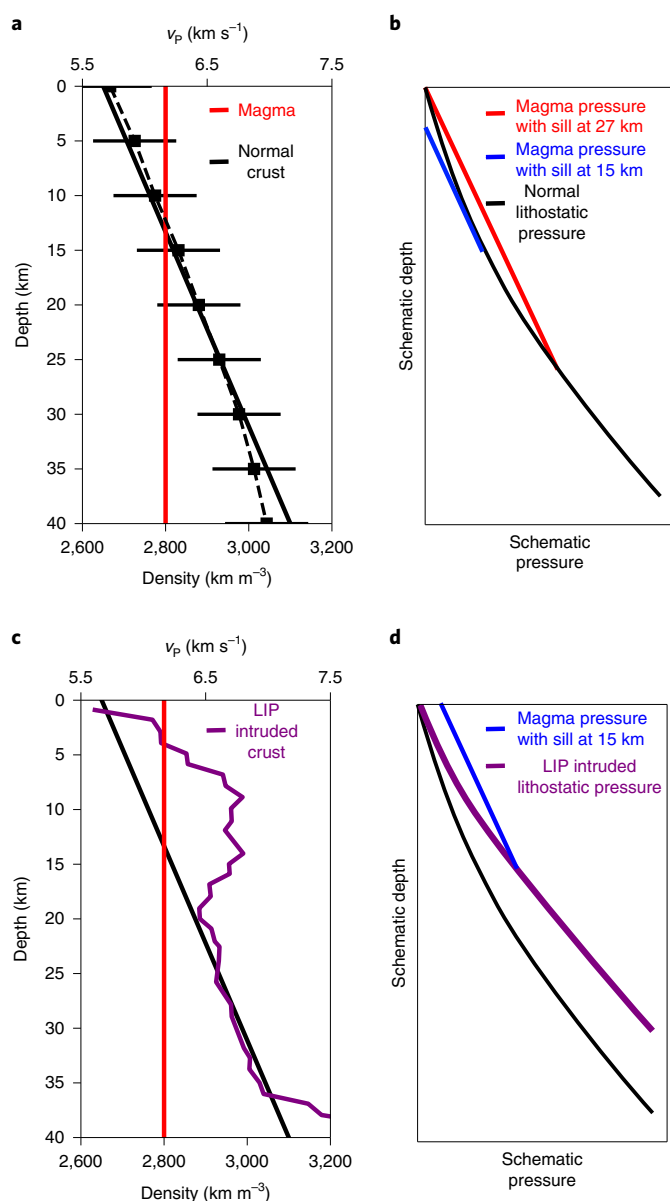
Fig. 2 | Relationships between seismic velocities, densities and pressures in typical continental crust and the crust under part of the Deccan Traps LIP. a,b, Typical continental crust. **a,** Average continental P-wave velocity (dashed) from ref. [41] with the density assuming a linear relation between velocity and density. The solid line shows the density assumed in the model. Magma density is from ref. [42]. **b,** The black line shows lithostatic pressure for the density structure given by the solid line in **a**. The red line shows static pressure in a column of magma that just reaches the surface, and the blue line shows the same for a column of magma with lithostatic pressure at a depth of 15 km. **c,d,** Crust under part of the Deccan Traps LIP. **c,** P-wave velocity and density profiles beneath the Deccan Traps are converted from refs. [13,15,18] using a v_S to v_P relationship (ref. [51]). **d,** The purple line shows lithostatic pressure for the LIP-intruded crustal density from **c**. The blue line shows that for densified crust a sill at a depth of 15 km has more than enough pressure to supply eruptions. Schematic depth and pressure are shown so the difference between the lithostatic pressure and magma pressure is visible.

Here we discuss a numerical model that builds on a recent 'multisill' approach[44]. The model assumes that Moho-level magma reservoirs[36] feed crustal sill intrusions. A new feature of our model

is that it explicitly determines the depth of each sill intrusion based on how earlier sills changed the thermal and compositional structure of the crust. The onset of a shift of LIP magma emplacement from mostly intrusion to mostly large-volume eruptions is assumed to be established when two necessary conditions are met: first, the overburden of an active sill is, on average, denser than the melt; second, the upwardly migrating magma from the Moho-level reservoir and the active sill is not intruded laterally before reaching the surface. The model also assumes that the magma flux follows a Gaussian function in time and that magma solidifies shortly after emplacement. This solidification releases most CO_2 dissolved in the magma into the atmosphere. A standard long-term ocean–atmosphere–sediment carbon cycle reservoir model (LOSCAR)[45] was used to compute the effect of this CO_2 flux on global temperatures (see Methods for details).

The system of crustal magma sill intrusion develops in four stages, as illustrated in Fig. 3. At stage one, the first sills are intruded into the mid-crust, and warm the country rock and densify the intruded region. As the melt supply increases, sills intrude at progressively shallower depths. The average density of the overburden of the intruding sills remains less than the magma density, so there are no major eruptions. Meanwhile, CO_2 exsolves from the cooling and solidifying melt and is added to the atmosphere.

Between stages (1) and (2), a series of sills are emplaced upward between sill 1 and sill 2 as the melt flux increases. Significant heat is added to the crust at depths at which the sills intrude. Again, there is no eruption at this time as the average density of the overburden is still less than that of magma. At stage (3), as a series of sills intrude into the mid-to-upper crust, hydrothermal circulation that transports heat to the surface increases its vigour due to the higher thermal gradient and permeability that result from fractures induced by sill intrusions. However, the magma flux begins to decrease. Sill intrusions cannot exist at shallower depths than the depth at which heat lost to the surface is sustained by heat input from sill intrusions. Still no eruptions occur because the density of magma is still greater than the depth-averaged density of crust above the intruding sill.

From stage (3) to stage (4), the magma supply wanes but the hydrothermal circulation is still vigorous. The intruded upper crust cools, solidifies and becomes denser and stronger. The resistance to sill intrusion increases at shallow depths. Sills intrude deeper into the hotter and weaker crust (Fig. 3, sill 4). The average overburden density is now higher than that of the fluid magma. As the densified and stronger crust prevents lateral intrusions above the active sill, magma from the intruding sill can directly erupt to the surface.

The time lag between the onset of predicted warming and the main extrusive phase depends on several model parameters, which include: the magma flux through time; the radii of the magma sills; the initial thermal, compositional and density structures of the crust and the efficiency of hydrothermal heat transport in the shallow crust. Without assuming a vigorous effective hydrothermal cooling of the shallow crust, the modelled time lag between the intrusive and extrusive onsets is longer than that observed. Fig. 4a–c shows results from one model run that predicts a global warming signal similar to that seen for the Deccan Traps. The coupled LOSCAR model indicates that the intrusive CO_2 initiates about 2 °C of global warming ~300 kyr before the main phase of LIP volcanism. Compared with the Deccan Traps, CRBG is smaller in size but its crustal temperature was probably greater. By lowering the maximum sill-thickening rate from 15 to 10 cm yr^{-1}, increasing the upper crustal thermal gradient by 5 K km^{-1} and increasing the rate of advective cooling by 20%, we obtained results that fit the CRBG and MCO cases (Fig. 4d–f).

Implications for LIP emplacements and global warming

Our model suggests that intrusion-induced densification of the continental crust has to occur before the large-scale continental
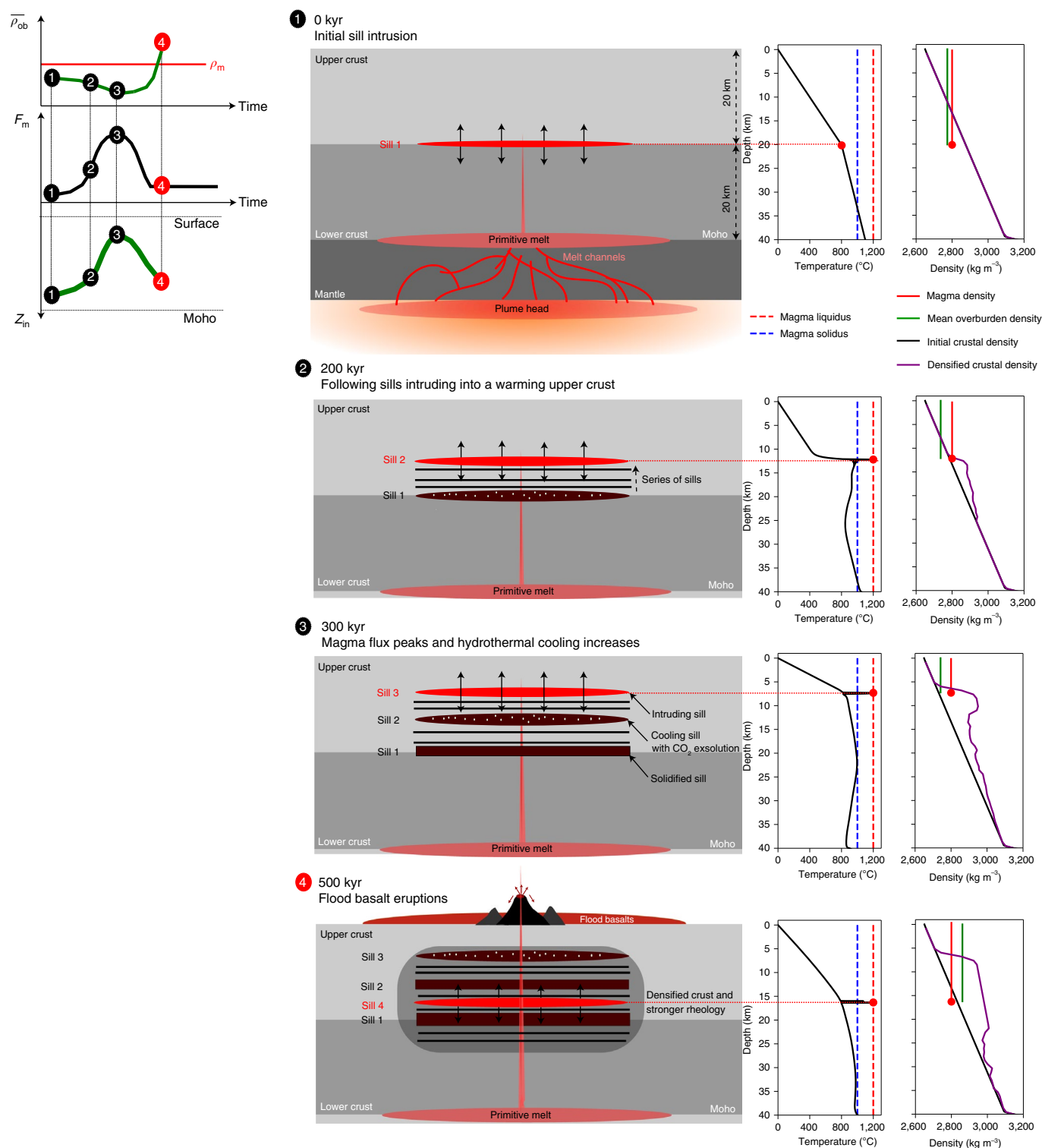
Fig. 3 | One-dimensional (1D) thermomechanical model results showing the changes in crustal temperatures and densities due to evolving sill intrusions. Z_{in} is the intrusion depth, F_m is the magma flux, $\overline{\rho_{ob}}$ is average density of the overburden and ρ_m is the magma density. (1)–(4) correspond to the stages of system development described in the text.

flood basalt main-phase eruptions. Massive CO_2 degassing from the solidifying intrusions can cause significant global warming. This provides an explanation for the time lag between climate warming and the flood basalt flux. It may also explain why the main phase of several mass extinctions predates the onset of their related LIP eruptions[5,23,46].

Several observations support our model. A key assumption that CO_2 exsolves at depth as magma crystallizes is supported by the recent melt inclusion studies of LIP lavas, which indicate the mid-to-lower crustal exsolution of abundant CO_2 (refs. [33,34]). Another requirement of the model is that magma sill intrusions should migrate upward and downward within several hundred
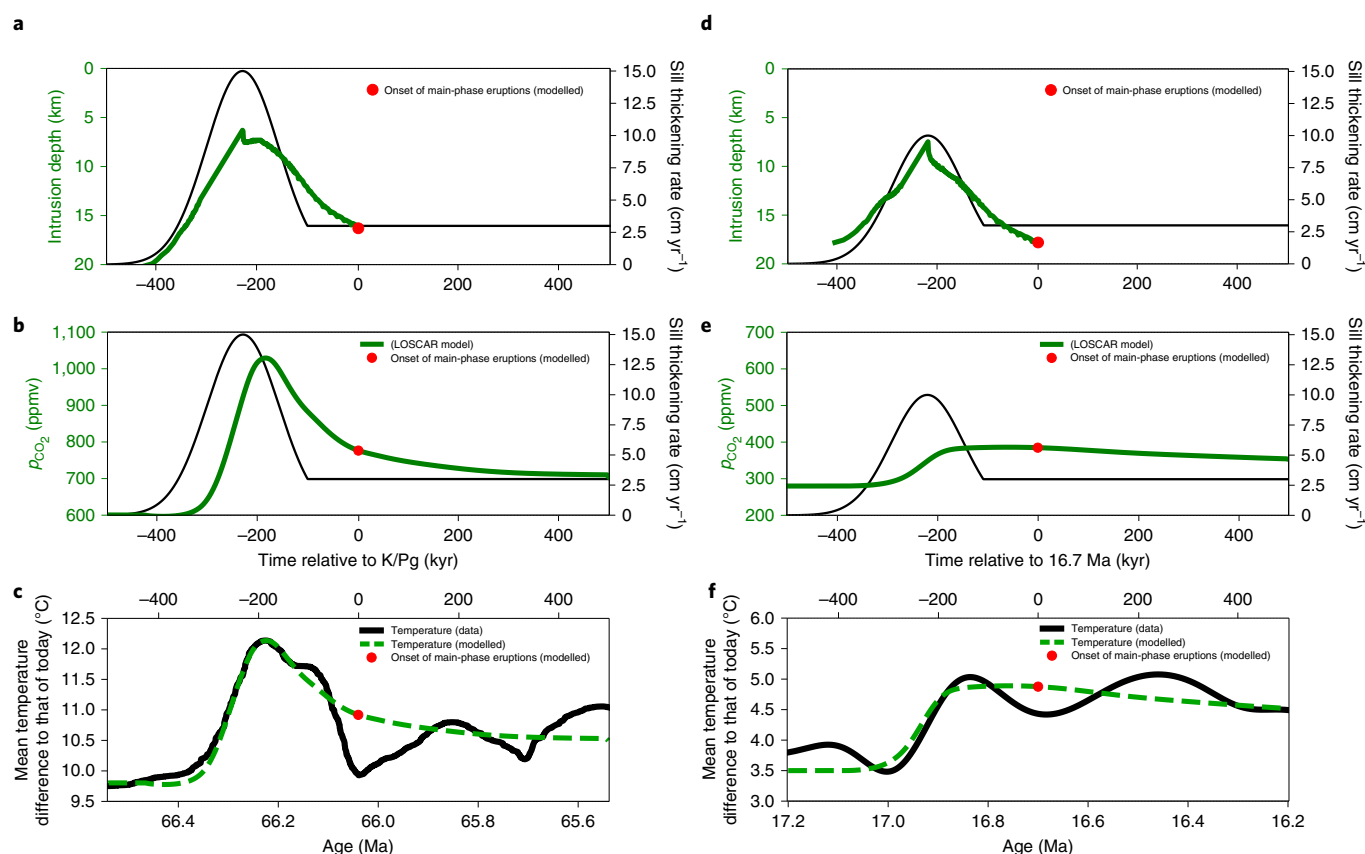
Fig. 4 | Time series of modelled global temperature variations and onsets of the main-phase eruptions of Deccan Traps and CRBG. a–f, Time series for the main-phase eruptions of the Deccan Traps around the K/Pg (**a–c**) and of CRBG and MCO (**d–f**). **a,d,** Sill intrusion depth and the timing of transition from mostly intrusion to main-phase eruptions, predicted by the thermomechanical model described in Methods, given the indicated melt flux with time. The CRBG case (**d**) has a lower peak sill thickening rate of 10 cm yr⁻¹. **b,e,** Global averaged atmospheric CO_2 concentration with time predicted by the LOSCAR climate model. **c,f,** global temperature change predicted by the LOSCAR model on top of climate data (Fig. 1) and with the modelled timing of the onsets of main-phase eruptions. See the Supplementary Information for details of the LOSCAR model set-up.

thousand years to densify the crust and induce the onset of major eruptions. That even modestly sized mantle plumes can produce shallow magma emplacement is evidenced by seismic data, which indicates a large volume of partially molten crust less than 10 km below Yellowstone, where high heat flux, up to 2,000 mW m⁻², is also reported[31].

Most earlier studies assume that the main climatic effect of LIPs results from the CO_2 liberated by surface lava flows. As the amount of CO_2 released directly from flood basalts is insufficient to produce the observed global warming, several groups invoke sources of extra carbon, which include 'cryptic' degassing[47] either by the sill intrusion heating of carbon-rich sedimentary strata[30] or by a carbon-rich plume that melts and releases CO_2 deep in the mantle[48]. However, cryptic degassing through carbonate intrusion is not relevant for the Deccan Traps or CRBG given the regional geology. Besides requiring anomalously high carbon concentrations, these models do not address the time lag between global warming and the major LIP eruption phase.

Hull et al.[3] assume that all the CO_2 comes from erupted lava and ran similar LOSCAR models across the K/Pg boundary. They conclude that the best fit to the climate data requires at least 50% of the volume of the Deccan flows to occur before the K/Pg boundary. Neither the ⁴⁰Ar/³⁹Ar (ref. [6]) nor the U–Pb (ref. [7]) geochronology model meet that condition. Hull et al.[3] suggest that "if the U–Pb model is correct … then most CO_2 outgassing must have preceded lava emplacement by several hundred thousand years", which is consistent with our model results. Hence, neither the U–Pb nor the

⁴⁰Ar/³⁹Ar models should be discounted at this time because warming could depend more on outgassing during the intrusions.

We agree with previous workers[36,37,49] that magma has to be less dense than the overlying crust to allow LIP eruptions. Earlier groups argue that this is accomplished by decreasing the magma density when exsolved volatiles are retained in the magma[36,37,49], whereas we assume it occurs by increasing the crustal density via intrusions. Both processes are likely to occur, but only the intrusion densification model explains the observations of global warming preceding the main phase of eruptions for two of the best-studied LIPs.

Online content

Any methods, additional references, Nature Research reporting summaries, source data, extended data, supplementary information, acknowledgements, peer review information; details of author contributions and competing interests; and statements of data and code availability are available at https://doi.org/10.1038/s41561-022-00939-w.

References

1. Coffin, M. F. & Eldholm, O. Large igneous provinces: crustal structure, dimensions, and external consequences. *Rev. Geophys.* **32**, 1–36 (1994).
2. Black, B. A. & Gibson, S. A. Deep carbon and the life cycle of large igneous provinces. *Elements* **15**, 319–324 (2019).

3. Hull, P. M. et al. On impact and volcanism across the Cretaceous–Paleogene boundary. *Science* **367**, 266–272 (2020).

4. Courtillot, V. E. & Renne, P. R. On the ages of flood basalt events. *C. R. Geosci.* **335**, 113–140 (2003).

5. Kasbohm, J., Schoene, B. & Burgess, S. in *Large Igneous Provinces: A Driver of Global Environmental and Biotic Changes* (eds Ernst, R. E., Dickson, A. J. & Bekker, A.) 27–82 (AGU, 2021).

6. Sprain, C. J. et al. The eruptive tempo of Deccan volcanism in relation to the Cretaceous–Paleogene boundary. *Science* **363**, 866–870 (2019).

7. Schoene, B. et al. U–Pb constraints on pulsed eruption of the Deccan Traps across the end-Cretaceous mass extinction. *Science* **363**, 862–866 (2019).

8. Richards, M. A. et al. Triggering of the largest Deccan eruptions by the Chicxulub impact. *Geol. Soc. Am. Bull.* **127**, 1507–1520 (2015).

9. Holbourn, A., Kuhnt, W., Kochhann, K. G. D., Andersen, N. & Sebastian Meier, K. J. Global perturbation of the carbon cycle at the onset of the Miocene Climatic Optimum. *Geology* **43**, 123–126 (2015).

10. Kasbohm, J. & Schoene, B. Rapid eruption of the Columbia River flood basalt and correlation with the mid-Miocene climate optimum. *Sci. Adv.* **4**, eaat8223 (2018).

11. Westerhold, T. et al. An astronomically dated record of Earth's climate and its predictability over the last 66 million years. *Science* **369**, 1383–1387 (2020).

12. Crisp, J. A. Rates of magma emplacement and volcanic output. *J. Volcanol. Geotherm. Res.* **20**, 177–211 (1984).

13. Pandey, O. P. Deccan Trap volcanic eruption affected the Archaean Dharwar craton of southern India: seismic evidences. *J. Geol. Soc. India* **72**, 510–514 (2008).

14. Kumar, P., Tewari, H. C. & Khandekar, G. An anomalous high-velocity layer at shallow crustal depths in the Narmada zone, India. *Geophys. J. Int.* **142**, 95–107 (2000).

15. Ravi Kumar, M. & Mohan, G. Mantle discontinuities beneath the Deccan volcanic province. *Earth Planet. Sci. Lett.* **237**, 252–263 (2005).

16. Bhattacharji, S., Sharma, R. & Chatterjee, N. Two- and three-dimensional gravity modeling along western continental margin and intraplate Narmada–Tapti rifts: its relevance to Deccan flood basalt volcanism. *J. Earth Syst. Sci.* **113**, 771–784 (2004).

17. Kumar, S., Gupta, S., Kanna, N. & Sivaram, K. Crustal structure across the Deccan Volcanic Province and Eastern Dharwar craton in south Indian shield using receiver function modelling. *Phys. Earth Planet. Inter.* **306**, 106543 (2020).

18. Rohilla, S., Kumar, M. R., Rao, N. P. & Satyanarayana, H. V. S. Shear-wave velocity structure of the Koyna–Warna region, Western India, through modeling of P-receiver functions. *Bull. Seismol. Soc. Am.* **108**, 1314–1325 (2018).

19. Patro, P. K. & Sarma, S. V. S. Evidence for an extensive intrusive component of the Deccan Large Igneous Province in the Narmada Son Lineament region, India, from three dimensional magnetotelluric studies. *Earth Planet. Sci. Lett.* **451**, 168–176 (2016).

20. Catchings, R. D. & Mooney, W. D. Crustal structure of the Columbia Plateau: evidence for continental rifting. *J. Geophys. Res. Solid Earth* **93**, 459–474 (1988).

21. Gao, H., Humphreys, E. D., Yao, H. & van der Hilst, R. D. Crust and lithosphere structure of the northwestern US with ambient noise tomography: terrane accretion and Cascade arc development. *Earth Planet. Sci. Lett.* **304**, 202–211 (2011).

22. Gao, H. Crustal seismic structure beneath the source area of the Columbia River flood basalt: bifurcation of the Moho driven by lithosphere delamination. *Geophys. Res. Lett.* **42**, 9764–9771 (2015).

23. Liu, Y., Li, L., van Wijk, J., Li, A. & Fu, Y. V. Surface-wave tomography of the Emeishan large igneous province (China): magma storage system, hidden hotspot track, and its impact on the Capitanian mass extinction. *Geology* **49**, 1032–1037 (2021).

24. Cherepanova, Y., Artemieva, I. M., Thybo, H. & Chemia, Z. Crustal structure of the Siberian craton and the West Siberian basin: an appraisal of existing seismic data. *Tectonophysics* **609**, 154–183 (2013).

25. Ryberg, T. et al. Crustal structure of northwest Namibia: evidence for plume–rift–continent interaction. *Geology* **43**, 739–742 (2015).

26. Cashman, K. V., Sparks, R. S. J. & Blundy, J. D. Vertically extensive and unstable magmatic systems: a unified view of igneous processes. *Science* **355**, eaag3055 (2017).

27. Ernst, R. E., Liikane, D. A., Jowitt, S. M., Buchan, K. L. & Blanchard, J. A. A new plumbing system framework for mantle plume-related continental large igneous provinces and their mafic–ultramafic intrusions. *J. Volcanol. Geotherm. Res.* **384**, 75–84 (2019).

28. Moore, N. E., Grunder, A. L. & Bohrson, W. A. The three-stage petrochemical evolution of the Steens Basalt (southeast Oregon, USA) compared to large igneous provinces and layered mafic intrusions. *Geosphere* **14**, 2505–2532 (2018).

29. Rosenthal, A., Hauri, E. H. & Hirschmann, M. M. Experimental determination of C, F, and H partitioning between mantle minerals and carbonated basalt, CO_2/Ba and CO_2/Nb systematics of partial melting, and the CO_2 contents of basaltic source regions. *Earth Planet. Sci. Lett.* **412**, 77–87 (2015).

30. Svensen, H. et al. Release of methane from a volcanic basin as a mechanism for initial Eocene global warming. *Nature* **429**, 542–545 (2004).

31. Huang, H.-H. et al. The Yellowstone magmatic system from the mantle plume to the upper crust. *Science* **348**, 773–776 (2015).

32. Lee, H. et al. Massive and prolonged deep carbon emissions associated with continental rifting. *Nat. Geosci.* **9**, 145–149 (2016).

33. Capriolo, M. et al. Deep CO_2 in the end-Triassic Central Atlantic Magmatic Province. *Nat. Commun.* **11**, 1670 (2020).

34. Hernandez Nava, A. et al. Reconciling early Deccan Traps CO_2 outgassing and pre-KPB global climate. *Proc. Natl Acad. Sci. USA* **118**, e2007797118 (2021).

35. Mutch, E. J. F., Maclennan, J., Holland, T. J. B. & Buisman, I. Millennial storage of near-Moho magma. *Science* **365**, 260–264 (2019).

36. Karlstrom, L. & Richards, M. On the evolution of large ultramafic magma chambers and timescales for flood basalt eruptions. *J. Geophys. Res. Solid Earth* **116**, B08216 (2011).

37. Black, B. A. & Manga, M. Volatiles and the tempo of flood basalt magmatism. *Earth Planet. Sci. Lett.* **458**, 130–140 (2017).

38. Ridley, V. A. & Richards, M. A. Deep crustal structure beneath large igneous provinces and the petrologic evolution of flood basalts. *Geochem. Geophys. Geosyst.* **11**, Q09006 (2010).

39. Hooft, E. E. & Detrick, R. S. The role of density in the accumulation of basaltic melts at mid-ocean ridges. *Geophys. Res. Lett.* **20**, 423–426 (1993).

40. Buck, W. R., Carbotte, S. M. & Mutter, C. Controls on extrusion at mid-ocean ridges. *Geology* **25**, 935–938 (1997).

41. Christensen, N. I. & Mooney, W. D. Seismic velocity structure and composition of the continental crust: a global view. *J. Geophys. Res.* **100**, 9761–9788 (1995).

42. Stolper, E. & Walker, D. Melt density and the average composition of basalt. *Contrib. Mineral. Petrol.* **74**, 7–12 (1980).

43. White, R. S. & McKenzie, D. Mantle plumes and flood basalts. *J. Geophys. Res. Solid Earth* **100**, 17543–17585 (1995).

44. Annen, C., Blundy, J. D. & Sparks, R. S. J. The genesis of intermediate and silicic magmas in deep crustal hot zones. *J. Petrol.* **47**, 505–539 (2006).

45. Zeebe, R. E., Zachos, J. C. & Dickens, G. R. Carbon dioxide forcing alone insufficient to explain Palaeocene–Eocene Thermal Maximum warming. *Nat. Geosci.* **2**, 576–580 (2009).

46. Wignall, P. B. Large igneous provinces and mass extinctions. *Earth Sci. Rev.* **53**, 1–33 (2001).

47. Armstrong McKay, D. I., Tyrrell, T., Wilson, P. A. & Foster, G. L. Estimating the impact of the cryptic degassing of large igneous provinces: a mid-Miocene case-study. *Earth Planet. Sci. Lett.* **403**, 254–262 (2014).

48. Sobolev, S. V. et al. Linking mantle plumes, large igneous provinces and environmental catastrophes. *Nature* **477**, 312–316 (2011).

49. Lange, R. A. Constraints on the preeruptive volatile concentrations in the Columbia River flood basalts. *Geology* **30**, 179–182 (2002).

50. Schoene, B., Eddy, M. P., Keller, C. B. & Samperton, K. M. An evaluation of Deccan Traps eruption rates using geochronologic data. *Geochronology* **3**, 181–198 (2021).

51. Brocher, T. M. Empirical relations between elastic wavespeeds and density in the Earth's crust. *Bull. Seismol. Soc. Am.* **95**, 2081–2092 (2005).

Methods

To consider the timing between flood basalt volcanism and global climate response due to the emplacement of a LIP, we developed two versions of a thermomechanical sill intrusion model. For a given variable magma flux with initial crustal thermal, density and compositional structures, these models estimate temporal changes of the density and thermal structure of continental crust. These changes govern the predicted onset of the main phase of flood basalt volcanism. The model CO_2 degassing flux was then used as an input variable to LOSCAR[45,52] for its climatic response.

As described in the main text, a key assumption of the model is that the initiation of the main phase of flood basalt volcanism is declared when two conditions are met: first, the overburden of an active sill is, on average, denser than the melt; second, the upwardly migrating magma from the shallowest active sill is not intruded laterally before reaching the surface. The first condition is determined by the crustal density structure and the depth of the intruding sill and the second condition is controlled by the thermomechanical state of the crust.

A sill intrusion of basaltic magma into the continental crust affects both the thermomechanical state and the density structure of the crust, which further affects where the following sill intrusions are most likely to happen and whether the two necessary conditions are met for large-scale flood basalt eruptions to occur. Here we first give details of a simplified analytical crustal model and then a more complex multisill model that treat such intrusion-related crustal changes. The purpose of these models is to assess whether a model with reasonable assumptions and parameter values can produce significant magma intrusion followed by main-phase flood basalt eruptions several hundred thousand years later. A key output is the predicted time lag between the onset of a significant global warming signal related to CO_2 release from a solidifying magma intrusion and the onset of the main phase of flood basalt extrusion. Before describing the simplified analytical model and the more complex multisill model, we describe the assumptions and parameter values common to both approaches. Note that the geochemical trends through the history of LIP eruptions are complex: as lavas become increasingly mantle derived in the Deccan Traps[8,53–55] and the Chifeng igneous province[56], they show an increasing crustal contamination in the CRBG[57,58]. Our model therefore does not make predictions on the petrology of LIP extrusive units.

Common model features. *One-dimensional thermal model.* We treated crustal magma emplacement as numerous discrete basaltic sill intrusions similar to the treatment in previous models[44,59]. We assumed that each magma sill is emplaced instantly at its liquidus temperature and only accounted for the vertical transfer of heat, mass and stress. The assumption of instant emplacement is reasonable because thermal diffusion is much slower than the propagation of a sill intrusion. Considering only the changes in the vertical z-axis direction is justifiable when a sill has a lateral dimension much larger than its thickness and depth so that the lateral heat transport is negligible. This wide but thin geometry of the sills also allow us to neglect flexural response due to the loads of intrusions, which is small when compared with the vertical movement of the isostatic adjustment. The initial crustal thickness is taken to be close to the global average of 40 km (ref. [41]). The surface is always kept at 0 °C. The convection of water through pore spaces in the shallow crust is considered to enhance heat transfer and we followed other workers[60,61] who approximated this effect by taking the effective conductivity of the crust to be multiplied by a factor Nu (after the Nusselt number for steady-state convection).

The evolution of temperatures with depth and time t are described by the 1D heat equation:

$$\frac{\partial T(z,t)}{\partial t} = \mathrm{Nu}\,(z,t)\,\kappa\,\frac{\partial^2 T}{\partial z^2} - \nu(t)\frac{\partial T}{\partial z} + \frac{H_m}{\rho(z)C_p} \quad (1)$$

where $T(z, t)$ is temperature as a function of depth z (positive downward) and time t, $\mathrm{Nu}(z, t)$ is a dimensionless prefactor that describes an enhanced heat transfer efficiency as a function of depth z and time t, thermal diffusivity $\kappa = 10^{-6}\,\mathrm{m}^2\,\mathrm{s}^{-1}$, $\nu(t)$ is the downward advection velocity of the crust beneath the intruding sill and is equal to the sill thickening rate $F_m(t)$, which is also the magma supply flux per unit area. H_m (W m^{-3}) is the heat liberation or storage rate, which accounts for the heat liberated on the cooling and solidification of basaltic melt and the heat stored on melting of solid basalt. $\rho(z)$ is the density and $C_p = 1,400\,\mathrm{J\,kg^{-1}\,K^{-1}}$ is the specific heat. The magma in the sills was assumed to solidify shortly after emplacement as the timescale for thermal diffusion of a 100-m-thick sill is two orders of magnitude shorter than the observed time lag between the onsets of warming and eruption. Here, for simplicity, we ignore the crustal radiogenic heat production.

Assumed magma flux. The flux of magma added to the crust is taken to vary in time according to a Gaussian function with a constant tail:

$$F_m(t) = \begin{cases} F_m^0 \exp[-(t-t_0)^2/2c^2], & t < t_1 \\ F_m^1, & t \geq t_1 \end{cases} \quad (2)$$

where F_m^0 is the maximum flux at time t_0 and F_m^1 is the constant flux after time t_1 when $t > t_0$ and $F_m^1 = F_m^0 \exp\left[-(t_1-t_0)^2/2c^2\right]$, where c controls the width in time of the Gaussian function. $F_m^0 \exp\left[-(t-t_0)^2/2c^2\right]$ represents the crustal

magma intrusion flux being generated by a mantle plume head and F_m^1 represents a plume-tail-induced magma flux. In our 1D treatment, the flux has units of volume flux per area (m s^{-1}).

Assuming a radius R of the circular disk-like sill intrusions, the volume flux of magma intrusion is then easily calculated as $V_m(t) = F_m(t)\,\pi R^2$. R is assumed to be 1,000 times the thickness of the sills emplaced during one modelled intrusion episode. During the eruption phase, R is assumed to be 110 km (50 km for CRBG-MCO) which yields an averaged eruption rate of 1.1404 km^3 yr^{-1} (0.2356 km^3 yr^{-1} for CRBG-MCO). Studies on the concentrations of Ba and Nb in picrites suggest a 0.1~2 wt% of CO_2 concentration in the original mantle-derived magma[62,63] and we assumed this concentration to be 1.5 wt% for the multisill model and 1.2 wt% for the analytical model, with degassing efficiencies of 55% for the intrusion and 70% for the extrusion[2,64] and, depending on the timing of the declaration of the main phase of the flood basalt eruptions, the model results in a time series of CO_2 outgassing flux. The modelled CO_2 outgassing flux was then used as an input into the multibox long-term carbon cycle and climatic response model described below.

The initial density structure of continental crust $\rho_c(z, t=0)$ was simplified according to ref. [41] with a linear fit that increases from 2,650 kg m^{-3} at the surface to 3,100 kg m^{-3} at the Moho depth $L_M = 40$ km (Fig. 2a). The crustal density structure $\rho_c(z,t)$ changes with intrusions of fluid magma of 2,800 kg m^{-3}, which increases to a depth-dependent density of $\rho_s(z) = 2,900 + 200 \times (\frac{z}{L_M})$ kg m^{-3} for solidified basalt (Fig. 3).

LOSCAR climate model. We used the LOSCAR version 2.0.4.3[45,52] to simulate the global temperature response to the CO_2 outgassing during LIP emplacements. Our model set-up and parameters followed those of refs. [3,65] for the Deccan Traps case and ref. [47] for the CRBG–MCO case. Specifically, we set $[Mg^{2+}] = 42$ mmol kg^{-1} (46 for CRBG–MCO) and $[Ca^{2+}] = 21$ mmol kg^{-1} (14.8 for CRBG-MCO) as equilibrium constants for the carbonate chemistry calculations for K/Pg (MCO) seawater. Sediment depth resolution was divided with the standard 500 m interval rather than the previously used more finely subdivided 100 m depth intervals because both show similar results but the models with a finer resolution take more than 20 times longer. The exponential constant (n_{si}) used in the silicate weathering feedback equation was 0.6 (0.2 for CRBG–MCO) following refs. [3,47,65]. Note that the higher n_{si} during the end Cretaceous results in a faster draw down of p_{CO_2} (Fig. 4b,e). A pre-event baseline p_{CO_2} of 600 ppm (280 for CRBG–MCO) was used following refs. [3,47,65] by restarting the model with precalculated steady-state model parameters. The calculated global temperature responses due to CO_2 outgassing from the LIP emplacement are presented in Fig. 4c,f. Note that an exact curve fitting of the global temperature could be possible but is not the point of this study; rather, we here try to demonstrate quantitatively with reasonable and well-studied controlling parameters that our coupled sill intrusion and LOSCAR models are capable of predicting similar patterns of climate and LIP behaviours when compared with those of the observations.

Analytical sill intrusion model. To demonstrate the plausibility of our conceptual model for a significant intrusion before the continental flood basalt extrusion, we first considered a simplified analytical version based on a balance of thermal energy. The temperature structure of the crust above the intruding sills was assumed to reach a steady state ($\delta T(z, t)/\delta t = 0$) immediately as the magma supply flux changes. This is purely for the sake of analytical simplification and induces an inaccuracy in the time for temperature changes, which is treated more realistically in the multisill model described later. For this approach, the domain of interest is between the surface and the top of an intruding sill so we neglected the effects of downward crustal advection beneath the intruding sill ($\nu = 0$). Over this domain, we only considered the liberation of heat ($H_m/(\rho(z)\,C_p)$) from the sill as a bottom heat flux boundary condition and that temperature correlates linearly with depth. The thermal equation (equation (1) then simplifies to:

$$Nu\,(z,t)\,\kappa\,\frac{\partial^2 T}{\partial z^2} = 0 \quad (3)$$

Integrating equation (3) with respect to the depth z and assuming that at the bottom boundary the heat flux (Q_{sill}) is sourced from the cooled and solidified sill with a constant Nu yields:

$$\mathrm{Nu} \times k\frac{\partial T}{\partial z} = Q_{sill} \quad (4)$$

where $k = \kappa \rho_t C_p = 3.3$ W mK^{-1} is the constant thermal conductivity of crustal rocks. The heat flux coming from the sill is taken to be:

$$Q_{sill} = F_m(t) \times \rho_f \left[L + (T_1 - T_s)\,C_p\right] \quad (5)$$

where $\rho_f = 2,800$ kg m^{-3} is the density of the fluid magma and $L = 4 \times 10^5$ J kg^{-1} is the latent heat of solidification, $T_s = 1,000$ °C is the magma solidus and $T_1 = 1,200$ °C is the magma liquidus. Applying a top boundary condition of $T(0,t) = 0$ °C and a moving bottom boundary condition of $T(Z_{in}, t) = T_s$, where Z_{in} is the evolving

sill-intrusion depth, we have a thermal gradient of $\delta T/\delta z = [T_s - T(0,t)]/Z_{in}$, which is plugged into equations (4) and (5) to determine the intrusion depth as:

$$Z_{in} = \frac{Nu \times k \times T_s}{F_m \rho_f [L + (T_1 - T_s) C_p]} \qquad (6)$$

For the example used here we assumed the plume head is controlled by $F_m^0 = 15 \text{ cm yr}^{-1}$, $t_0 = 170 \text{ kyr}$ and $c = 210\sqrt{2/\pi} \text{ kyr}$ followed by a plume tail of a constant $F_m^1 = 6 \text{ cm yr}^{-1}$ thickening rate. Extended Data Fig. 1a shows this example flux–time curve and Extended Data Fig. 1b shows the resulting variation of the intrusion depth given by equation (6).

This sill intrusion depth along with the density structure and an assumed critical overpressure for the initiation of eruptions $\Delta P_c = 10 \text{ MPa}$ (refs. [66–68]) determines whether magma can extrude subaerially or is intruded within the crust. We also assumed that deepening of sill intrusions is taken to imply the replacement of felsic continental crust with denser basaltic rocks. This densification of the crust then affects the depth at which magma in a sill can be erupted, which is termed as the 'level of eruptibility' (see main text). For extrusion to occur there has to be enough pressure in the magma sill to drive the magma to the surface. We assumed that the pressure in the magma sill is just the overburden pressure:

$$P_{OB}(Z_{in}, t) = \int_0^{Z_{in}} \rho_c(z,t) g \, dz \qquad (7)$$

where $\rho_c(z,t)$ is the crustal density profile and $g = 10 \text{ m s}^{-2}$ is the gravitational acceleration. We determined the magma eruptibility by whether the magma pressure head $P_h(z,t)$ at the surface ($z=0$) is larger than ΔP_c when sourced from the intruding sill at depth Z_{in}, where:

$$P_h(0, t) = P_{OB}(Z_{in}, t) - \rho_f g Z_{in} \qquad (8)$$

and this is equivalent to whether the overburden of the intruding sill is, on average, denser than the fluid magma to an extent that:

$$\bar{\rho}_{OB} > \rho_f + \Delta P_c / g Z_{in} \qquad (9)$$

where $\bar{\rho}_{OB}$ is the average overburden density.

Flood basalt eruptions could then happen in two ways. If the initial sills are deeper than the level of eruptibility then the condition is met so extrusion can occur. This might only happen when the initial magma flux is low and the intrusion is deep. Alternatively, a sill can move up to a depth much shallower than the level of eruptibility and then move downward as mafic magma in the sill cools and crystallizes. The sill intrusion moves downward as the flux of magma wanes and so the heat released by the magma decreases (as indicated in Extended Data Fig. 1b). We assumed that as the sill moves down it leaves behind intrusions with the density of solid basalt ($\rho_s(z)$). Now the overburden will be a mix of the initial low-density felsic crust and the higher-density solidified basalt. For a linear increase in the initial crustal density with depth (Fig. 2a), eruption can happen if:

$$Z_{in} \geq \frac{[\rho_s(Z_{inm}) + \rho_s(Z_{in}) - \rho_c(0) - \rho_c(Z_{inm})] \times Z_{inm} + 2\Delta P_c/g}{\rho_s(Z_{inm}) + \rho_s(Z_{in}) - 2\rho_f} \qquad (10)$$

where $Z_{inm} = \frac{Nu \times k \times T_s}{F_m^0 \rho_f [L + (T_1 - T_s) C_p]}$ is the minimum depth of the sill intrusions. When this condition is met, the magma pressure head at the surface is greater than ΔP_c, the critical pressure for initiating an eruption. Extended Data Fig. 1c shows how the magma pressure head varies in time. Once the timing of the onset of eruptions is determined, the model predicts a CO_2 degassing flux given the assumed magma concentration and degassing efficiencies. Using the CO_2 degassing flux as an input for the LOSCAR model, we calculated the global averaged atmospheric CO_2 concentration (Extended Data Fig. 1d) and temperature changes (Extended Data Fig. 1e) with time relative to the K/Pg boundary.

Multisill intrusion model. Our multisill intrusion model builds on previous numerical studies on the genesis and evolution of evolved crustal magmas[44,59]. By accounting for heat transfer and mass advection during repetitive sill intrusions, such models can quantify the changes in melt fraction and chemical compositions of the mantle-plume-induced magma that intrudes into the crust and mixes with crustal melts. As we are concerned with magma eruptibility rather than the chemical evolution of the system, our approach neglects chemical reactions of the magma and country rock. We focus on how changes in the crustal temperature and composition structures control the depth of sill intrusions and the density structure of the crust.

We argue in the main text that the depth of sill intrusion is important to determine whether magma is emplaced as intrusions or eruptions. Some studies assume an initial intrusion depth and that subsequent sills are emplaced over, under or within the earlier sills[44,59]. Other studies treat sill intrusion depths through time as stochastic processes[69,70]. As noted below, there is considerable evidence that the thermal structure of the crust has a large influence on the depth of sill intrusion. It is also clear that sill intrusion alters the crustal temperature structure and so can lead to an evolution of sill intrusion depths. As the crustal thermal structure does not respond instantaneously to changes in magmatic heat input, we

derived a time-dependent model that includes the diffusion and advection of heat, as described by equation (1). Before describing that model, we briefly review some recent studies of sill intrusion.

One of the most discussed ideas about sill-opening depth is that magmatic sills form at the 'level of neutral buoyancy' (LNB)[71]. This model assumes that crustal density increases with depth and that magma pools at the LNB at which the country rock density equals the magma density. This works in analogue laboratory models only if the 'crustal' material has negligible strength. However, many observations are at odds with the LNB concept (see refs. [72,73] and references therein). For example, this idea was tested by Hooft and Detrick[39] at mid-ocean ridges where seismic observations are of sufficient quality to determine the density structure above the magma-filled sills. They showed that the sills were located deeper than the LNB and they suggested that the strength of cold crust may be important. Some other studies imaged sill intrusions within lower-density sedimentary basins situated shallower than the LNB (for example, ref. [74] and references therein).

Some previous workers focused on the effects of mechanical strength changes across layers, which deflect a dyke into sills and hence the sill intrusion depth is determined by the location of the layer boundary[72,75]. A recent analogue model study summarizes that buoyancy pressure from the density contrast between the host rock and the injecting fluid, rigidity contrast and lateral compression are the major controls of the formation of sills[76]. Menand[72] reviewed existing models for sill emplacement depths as controlled by four major factors: (1) the buoyancy pressure due to the density contrast between the host rock and injecting fluid, (2) the rigidity contrast between strata, (3) the rheology control between warm ductile material and cold brittle material and (4) rotation of the deviatoric stress. These four factors can be further grouped into two major effects: either from buoyancy driving pressure controlled by density structures or from an effective resistant strength structure controlled by rigidity, rheology or stress state. All these factors are functions of temperature, which makes sill intrusion depth strongly dependent on thermal structures. Morgan and Chen[77] were the first to suggest that temperature was critical in controlling the depth of magma lenses at mid-ocean ridges. A recent 3D numerical modelling study of magma intrusion into the continental crust indicates that rheology and temperature of the host rocks are the key controls of how magma is emplaced[78]. Parsons et al.[79] first suggested that at large rheology contrasts, at which lower viscosity ductile layers are adjacent to a higher viscosity elastic layer, the least principal stress can be rotated vertically due to horizontal dyke opening. This rotation of the least principal stress can arrest the upward dyke propagation and induce lateral sill intrusions. A similar behaviour of dyke arrest is described by Buck[80] for rifts in which lithosphere-cutting dykes stop when the 'driving pressure' P_d (magma pressure minus the lithospheric stress normal to the dyke wall) is too small. This idea has also been used to explain analogue model results that show horizontal compressive stress can modify the path of a fluid crack from the vertical to the horizontal[81].

Here we assume that the sill intrusion depth evolves with the thermomechanical state and density structure following previous studies of the effects of thermal and stress states on sill formations[77,79]. For a column of magma that rises through the crust with a density that increases with depth, the magma overpressure P_d will be greatest at the LNB. However, if the rocks are cold and strong at this depth, the magma should not be able to force a sill to open. We estimated the resistance to sill opening as the resistance pressure (P_r). P_r depends partly on the host-rock temperature in that it controls whether magma will freeze before the sill intrusions can be open. P_r depends also on the composition and temperature, which control the horizontal stress ($\sigma_h(z,t)$) that acts normal to the vertical dyke-opening wall, because it controls where a vertical sill-feeding dyke is stopped due to a smaller driving pressure relative to that of the horizontal compressive stress. We assumed that a sill opens where the breakout pressure, namely, the difference between P_d and P_r ($P_{BK} = P_d - P_r$) is at a maximum ($P_{BK}(Z_{in}) = P_{BKm}$) (Extended Data Fig. 2).

The driving pressure for sill intrusion is computed by integrating the density difference between ρ_f and the ρ_c along a vertical melt migration conduit upward from the Moho level reservoir:

$$P_d(z) = \int_{Z_{moho}}^z (\rho_c - \rho_f) g \, dz \qquad (11)$$

This neglects any viscous pressure changes due to flow of the low viscosity primitive magma. For the driving pressure P_d, although the density difference between fluid magma and mantle country rock can be large, we assumed that the magma generated from the mantle plume gains negligible pressure head as it percolates through the low permeability melt channels in the upper mantle. Magma is assumed to then accumulate in the Moho-level magma reservoirs, as in previous studies of continental intrusions[36,37,73].

The resistance pressure P_r comes from two parts, namely, the thermal arrest pressure P_{TA} and the remaining (unrelaxed) dyke-opening-induced horizontal compressive stress σ_h. P_{TA} is the required magma pressure to sustain a thin but laterally wide sill intrusion. We estimated this pressure following previous 'thermal entry' length calculations[82,83], which consider the pressure needed to drive magma to flow a long distance before freezing. Here, we assumed a sill of thickness of

$w = 1\,m$ and a flow distance $R_{fz} = 200\,km$ before the magma fully freezes. The magma propagation in such a sill is assumed to be simplified as a thin channel flow with an average velocity of:

$$\bar{u} = \frac{w^2}{12\eta_m}\frac{dP}{dx} \qquad (12)$$

where the pressure gradient $dP/dx = P_{TA}/R_{fz}$, assuming a stable source pressure of P_{TA} (ref. [84]) and $\eta_m = 100\,Pa\,s$ is the assumed viscosity for the following fluid magma[85]. Then, the P_{TA} to drive a high aspect ratio thin channel sill intrusion before it freezes is:

$$P_{TA} = \frac{192 \times \kappa \times \eta_m \times R_{fz}^2 \times \lambda^2}{w^4} \qquad (13)$$

The freezing distance $R_{fz} = \bar{u}t_{fz}$ is calculated assuming a freezing time $t_{fz} = w^2/16\kappa\lambda^2$, which is the approximate time for a thin channel fluid magma flow a with thickness of w to freeze and λ is a dimensionless parameter determined by the temperature of the country rock at the sill intrusion depth $T(Z_{in})$ (refs. [83,86]) and is expressed in an implicit function only solved numerically:

$$\lambda = \frac{\exp\left(-\lambda^2\right)}{\pi^{\frac{1}{2}}S}\left[\frac{\theta}{\mathrm{erfc}\left(-\lambda\right)} - \frac{1-\theta}{\mathrm{erfc}\left(\lambda\right)}\right] \qquad (14)$$

where the dimensionless solidus temperature $\theta = [T_s - T(Z_{in})]/[T_l - T(Z_{in})]$, and the Stefan number $S = L/[C_p(T_l - T(Z_{in}))]$, where T_l is taken to be the intrusion temperature.

A vertical dyke is assumed to propagate quasi-periodically upward to feed sill intrusions from the magma reservoir at the base of the crust. As the dyke opens, it induces an instant elastic increase in the lateral compressive stress. If the dyke freezes in a cold and strong crust that behaves mainly elastically, the compressive stress increase can remain for a long period of time, which should inhibit vertical propagations of later dykes. If the dyke intrudes and freezes in a hotter and lower viscosity crust, the initial increase in lateral compressive stress can be effectively relaxed between the dyke events. Following the model of Parsons et al.[79], in which a sill can form at brittle–ductile transitions, we calculated the second part of the model resistant pressure as the temporally variable $\sigma_h(z,t)$ induced by a dyke opening. Assuming the crust behaves as a Maxwell viscoelastic material[84] with laboratory-constrained properties[87,88], we can estimate the amount of stress relaxation between intrusion events as functions of the temperature and assumed composition. When a dyke propagates vertically and opens laterally with the pressure distribution of magma driving pressure $P_d(z)$, it induces a compressive horizontal stress $\sigma_h(z, t=0) = P_d(z)$, which relaxes quickly at low viscosity regions. During the quasi-periodic intersessions of Δt (on the order of a few thousand years depending on the magma flux) between intrusions, this initial dyke-induced $\sigma_h(z, t=0)$ relaxed to $= \sigma_h(z, t=0=\Delta t)$ following a Maxwell relaxation stress relation[84]:

$$\sigma_h\left(z, t = \Delta t\right) = \sigma_h\left(z, t=0\right)\exp\left(-\frac{E\Delta t}{2\mu}\right) \qquad (15)$$

where the assumed Young's modulus $E = 30\,GPa$ (ref. [61]) and the strain-rate-independent viscosity of the country rock, μ, is calculated according to Chen and Morgan[60] with the power $n = 1$:

$$\mu = (3A)^{-1} \times \exp\left[\frac{Q}{nRT(Z_{in})}\right] \qquad (16)$$

where A is an empirical lab-determined viscosity prefactor, Q is the activation energy and $R = 8.314\,J\,mol^{-1}\,K^{-1}$ is the gas constant. For the upper crust, we used a lab-constrained equivalent Newtonian flow rule with $A = 0.0052\,MPa^{-1}\,s^{-1}$ (calculated from $2/3 \times 1.57 \times 10^{-3} \times 50^{0.41}$) and $Q = 131{,}500\,J\,mol^{-1}$ (ref. [87]). For the lower crust, for simplicity, A is scaled from the upper crust value to be five orders of magnitude smaller and hence the resulting viscosity is five orders of magnitude higher given the same temperature. For the 2 km of upper mantle, we applied the lab-constrained Newtonian rheology from ref. [88], in which the equivalent $A = 0.0006\,MPa^{-1}\,s^{-1}$ (calculated from $2/3 \times 10^6 \times (1 \times 10^{-4})^{-3} \times 1{,}000$) and $Q = 339{,}000\,J\,mol^{-1}$. For the solidified magma, we assumed an A value five orders of magnitude larger and hence the resulting viscosity is five orders of magnitude lower than that of the mantle given the same temperature. To prevent numerical localizations of sill intrusion at a specific grid, $T(Z_{in})$ is approximated with an average temperature of the country rocks near Z_{in} within a thermal diffusion length during one numerical time step of 1 kyr.

The initial vertical crustal temperature profile is taken to be piecewise linear with the initial upper crustal thermal gradient (0–20 km) of $dT/dZ = 40\,K\,km^{-1}$ (45 for the CRBG-MCO case) and a lower crustal thermal gradient (20–40 km) of $dT/dZ = 15\,K\,km^{-1}$ (Fig. 3). The magma supply flux (Fig. 4a) is assumed with $F_m^0 = 15\,cm\,yr^{-1}$ (10 for the CRBG-MCO case), $t_0 = 270\,kyr$ (280 for the CRBG–MCO case), $c = 90\sqrt{2/\pi}\,kyr$ and $F_m^1 = 3\,cm\,yr^{-1}$.

Numerically, heat equation (1) is discretized into a 1D array of grids, and is solved by forward finite-difference methods. We applied a semi-Lagrangian Crank–Nicolson algorithm[89] coupled with a one-half backward implicit step[90] to dampen the Crank–Nicolson error oscillations introduced by sharp temperature

corners from sill intrusions. As noted above, the average effect of hydrothermal circulation is simulated by increasing κ by a factor of Nu. The efficiency of the hydrothermal circulation should scale with the crustal permeability and thermal gradient. Hence, it should depend on the existence of interconnected cracks as well as on the crustal thermal condition. The upper crustal thermal gradient and fracture events should peak around the time when the magma flux $F_m(t)$ maximizes at t_0. Hence, we assume $Nu = 25$ from the surface to 20 km when $t \geq t_0$ and $Nu = 1$ otherwise (30 for the CRBG-MCO case). Note that measurements from Yellowstone indicate a surface heat flux of up to $2000\,mW\,m^{-2}$ (ref. [31]), which is nearly 30 times that of normal continental crust, $65\,mW\,m^{-2}$ (ref. [84]).

We determined the magma eruptibility by whether the magma pressure head at the surface ($P_h(0) = \int_{Z_{in}}^{0}(\rho_c - \rho_f)\,g\,dz$) was larger than the critical pressure (ΔP_c) to initiate an eruption when sourced from the intruding sill at depth Z_{in}:

$$P_h(0) > \Delta P_c \qquad (17)$$

This is equivalent to considering whether the average density of the overburden of an intruding sill is larger than the density of fluid magma to the extent of equation (9). During the initial phases when the sill is deep or when the crust densifies due to sill intrusions, the magma driving pressure at the surface $P_d(0)$ can be positive, which means magma from the Moho reservoir has the potential to erupt. However, we did not count the main phase of flood basalt eruptibility when magma is sourced from the Moho reservoir during the early phase of an LIP emplacement because the pressure head should be consumed by lateral sill intrusions into the initial weaker and lower density crust before the magma can reach the surface. We did not consider viscous resistances for the sill or dyke intrusions as they are negligible compared with the thermal arrest resistance from sill intrusions[85]. We also neglected temporal variations in the elastic overpressure from the magma reservoir, which can be responsible for finer timescale hiatuses in magma eruptions[36,37].

In the Supplementary Information, we include two videos of the multisill intrusion models (Supplementary Video 1 for the Deccan case and Supplementary Video 2 for the CRBG case), which illustrate in detail the changes in global temperature, sill intrusion depth, crustal temperature, density and pressures due to the sill intrusions. Note that for the assumed rheology parameters, the thermal arrest resistance pressure has the dominant effect on controlling the sill intrusion depths when the sills are moving upward into the weak lower part of the upper crust, but the dyke-related stress change becomes important during the sill-deepening phase (starting ~220 kyr before the onset of main-phase eruptions) as the sills open into stronger mafic intrusives. With our model formulation, the intruding depth is determined by considering both the density structure and the thermomechanical conditions, and hence is not always at the LNB.

Data availability
For Fig. 1a, the global temperature data are from ref. [3] (https://doi.org/10.1126/science.aay5055) and the Deccan Trap extrusive flux data are from Schoene et al.[50] (https://doi.org/10.5194/gchron-3-181-2021). For Fig. 2b, the global temperature data are from ref. [11] (https://doi.org/10.1126/science.aba6853) and the CRBG extrusive flux data are from ref. [10] (https://doi.org/10.1126/sciadv.aat8223). For Fig. 2, seismic velocity data are converted from data in ref. [13] (http://ischolar.info/index.php/JGSI/article/view/81438) and ref. [41] (https://doi.org/10.1029/95JB00259). These data, along with the plotting scripts to generate Figs. 1 and 2 are deposited at https://doi.org/10.5281/zenodo.6390698.

Code availability
Model input parameters, output data and the plotting scripts to generate Figs. 3 and 4 are deposited at https://doi.org/10.5281/zenodo.6390698. The sill intrusion code is available from the corresponding author upon request.

References
52. Zeebe, R. E. LOSCAR: Long-term Ocean–atmosphere–Sediment CArbon cycle Reservoir Model v2.0.4. *Geosci. Model Dev.* **5**, 149–166 (2012).
53. Beane, J. E., Turner, C. A., Hooper, P. R., Subbarao, K. V. & Walsh, J. N. Stratigraphy, composition and form of the Deccan Basalts, Western Ghats, India. *Bull. Volcanol.* **48**, 61–83 (1986).
54. Vanderkluysen, L., Mahoney, J. J., Hooper, P. R., Sheth, H. C. & Ray, R. The feeder system of the Deccan Traps (India): insights from dike geochemistry. *J. Petrol.* **52**, 315–343 (2011).
55. Basu, A. R., Saha-Yannopoulos, A. & Chakrabarty, P. A precise geochemical volcano-stratigraphy of the Deccan traps. *Lithos* **376–377**, 105754 (2020).
56. Yu, X., Lee, C. T. A., Chen, L. H. & Zeng, G. Magmatic recharge in continental flood basalts: insights from the Chifeng igneous province in Inner Mongolia. *Geochem. Geophys. Geosyst.* **16**, 2082–2096 (2015).
57. Wolff, J. A., Ramos, F. C., Hart, G. L., Patterson, J. D. & Brandon, A. D. Columbia River flood basalts from a centralized crustal magmatic system. *Nat. Geosci.* **1**, 177–180 (2008).
58. Reidel, S. P. & Barnett, D. B. Igneous rock associations 27. Chalcophile and platinum group elements in the Columbia River Basalt Group: a model for flood basalt lavas. *Geosci. Can.* **47**, 187–214 (2020).

59. Solano, J. M. S., Jackson, M. D., Sparks, R. S. J., Blundy, J. D. & Annen, C. Melt segregation in deep crustal hot zones: a mechanism for chemical differentiation, crustal assimilation and the formation of evolved magmas. *J. Petrol.* **53**, 1999–2026 (2012).

60. Chen, Y. & Morgan, W. J. A nonlinear rheology model for mid-ocean ridge axis topography. *J. Geophys. Res.* **95**, 17583 (1990).

61. Behn, M. D. & Ito, G. Magmatic and tectonic extension at mid-ocean ridges: 1. Controls on fault characteristics. *Geochem. Geophys. Geosyst.* **9**, Q08O10 (2008).

62. Kent, A. J. R. et al. Mantle heterogeneity during the formation of the North Atlantic Igneous Province: constraints from trace element and Sr–Nd–Os–O isotope systematics of Baffin Island picrites. *Geochem. Geophys. Geosyst.* **5**, Q11004 (2004).

63. Sobolev, A. V., Krivolutskaya, N. A. & Kuzmin, D. V. Petrology of the parental melts and mantle sources of Siberian trap magmatism. *Petrology* **17**, 253–286 (2009).

64. Hartley, M. E., Maclennan, J., Edmonds, M. & Thordarson, T. Reconstructing the deep CO_2 degassing behaviour of large basaltic fissure eruptions. *Earth Planet. Sci. Lett.* **393**, 120–131 (2014).

65. Henehan, M. J., Hull, P. M., Penman, D. E., Rae, J. W. B. & Schmidt, D. N. Biogeochemical significance of pelagic ecosystem function: an end-Cretaceous case study. *Phil. Trans. R. Soc. B* **371**, 20150510 (2016).

66. Rubin, A. M. Getting granite dikes out of the source region. *J. Geophys. Res. Solid Earth* **100**, 5911–5929 (1995).

67. Jellinek, A. M. & DePaolo, D. J. A model for the origin of large silicic magma chambers: precursors of caldera-forming eruptions. *Bull. Volcanol.* **65**, 363–381 (2003).

68. Townsend, M., Huber, C., Degruyter, W. & Bachmann, O. Magma chamber growth during intercaldera periods: insights from thermo-mechanical modeling with applications to Laguna del Maule, Campi Flegrei, Santorini, and Aso. *Geochem. Geophys. Geosyst.* **20**, 1574–1591 (2019).

69. Karakas, O., Degruyter, W., Bachmann, O. & Dufek, J. Lifetime and size of shallow magma bodies controlled by crustal-scale magmatism. *Nat. Geosci.* **10**, 446–450 (2017).

70. Dufek, J. & Bergantz, G. W. Lower crustal magma genesis and preservation: a stochastic framework for the evaluation of basalt–crust interaction. *J. Petrol.* **46**, 2167–2195 (2005).

71. Ryan, M. P. in *Magmatmatic Processes: Physicochemical Principles* (ed. Mysen, B. O.) 259–287 (The Geochemical Society, 1987).

72. Menand, T. Physical controls and depth of emplacement of igneous bodies: a review. *Tectonophysics* **500**, 11–19 (2011).

73. Rohrman, M. Intrusive large igneous provinces below sedimentary basins: an example from the Exmouth Plateau (NW Australia). *J. Geophys. Res. Solid Earth* **118**, 4477–4487 (2013).

74. Magee, C. et al. Lateral magma flow in mafic sill complexes. *Geosphere* **12**, 809–841 (2016).

75. Menand, T. The mechanics and dynamics of sills in layered elastic rocks and their implications for the growth of laccoliths and other igneous complexes. *Earth Planet. Sci. Lett.* **267**, 93–99 (2008).

76. Sili, G., Urbani, S. & Acocella, V. What controls sill formation: an overview from analogue models. *J. Geophys. Res. Solid Earth* **124**, 8205–8222 (2019).

77. Morgan, J. P. & Chen, Y. J. The genesis of oceanic crust: magma injection, hydrothermal circulation, and crustal flow. *J. Geophys. Res.* **98**, 6283 (1993).

78. Gorczyk, W. & Vogt, K. Intrusion of magmatic bodies Into the continental crust: 3-D numerical models. *Tectonics* **37**, 705–723 (2018).

79. Parsons, T., Sleep, N. H. & Thompson, G. A. Host rock rheology controls on the emplacement of tabular intrusions: implications for underplating of extending crust. *Tectonics* **11**, 1348–1356 (1992).

80. Buck, W. R. The role of magma in the development of the Afro-Arabian Rift System. *Geol. Soc. Lond. Spec. Publ.* **259**, 43–54 (2006).

81. Menand, T., Daniels, K. A. & Benghiat, P. Dyke propagation and sill formation in a compressive tectonic environment. *J. Geophys. Res.* **115**, B08201 (2010).

82. Spence, D. A. & Turcotte, D. L. Magma-driven propagation of cracks. *J. Geophys. Res. Solid Earth* **90**, 575–580 (1985).

83. Fialko, Y. A. & Rubin, A. M. Thermodynamics of lateral dike propagation: implications for crustal accretion at slow spreading mid-ocean ridges. *J. Geophys. Res. Solid Earth* **103**, 2501–2514 (1998).

84. Turcotte, D. L. & Schubert, G. *Geodynamics* (Cambridge Univ. Press, 2002).

85. Lister, J. R. & Kerr, R. C. Fluid-mechanical models of crack propagation and their application to magma transport in dykes. *J. Geophys. Res.* **96**, 10049 (1991).

86. Carslaw, H. S. & Jaeger, J. C. *Conduction of Heat in Solids* (Oxford Univ. Press, 1959).

87. Wang, J. N., Hobbs, B. E., Ord, A., Shimamoto, T. & Toriumi, M. Newtonian dislocation creep in quartzites: implications for the rheology of the lower crust. *Science* **265**, 1204–1206 (1994).

88. Hirth, G. & Kohlstedt, D. Rheology of the upper mantle and the mantle wedge: a view from the experimentalists. *Geophys. Monogr. Ser.* **138**, 83–105 (2003).

89. Spiegelman, M. & Katz, R. F. A semi-Lagrangian Crank–Nicolson algorithm for the numerical solution of advection–diffusion problems. *Geochem. Geophys. Geosyst.* **7**, Q04014 (2006).

90. Britz, D., Østerby, O. & Strutwolf, J. Damping of Crank–Nicolson error oscillations. *Comput. Biol. Chem.* **27**, 253–263 (2003).

Author contributions

X.T., advised by W.R.B., conducted the model experiments and both authors wrote the manuscript.

Competing interests

The authors declare no competing interests.

Additional information

Extended data is available for this paper at https://doi.org/10.1038/s41561-022-00939-w.

Supplementary information The online version contains supplementary material available at https://doi.org/10.1038/s41561-022-00939-w.

**Correspondence and requests for materials** should be addressed to Xiaochuan Tian.

Peer review information *Nature Geoscience* thanks Jennifer Kasbohm, Jon Blundy and the other, anonymous, reviewer(s) for their contribution to the peer review of this work. Primary Handling editor: Rebecca Neely, in collaboration with the *Nature Geoscience* team.

Reprints and permissions information is available at www.nature.com/reprints.
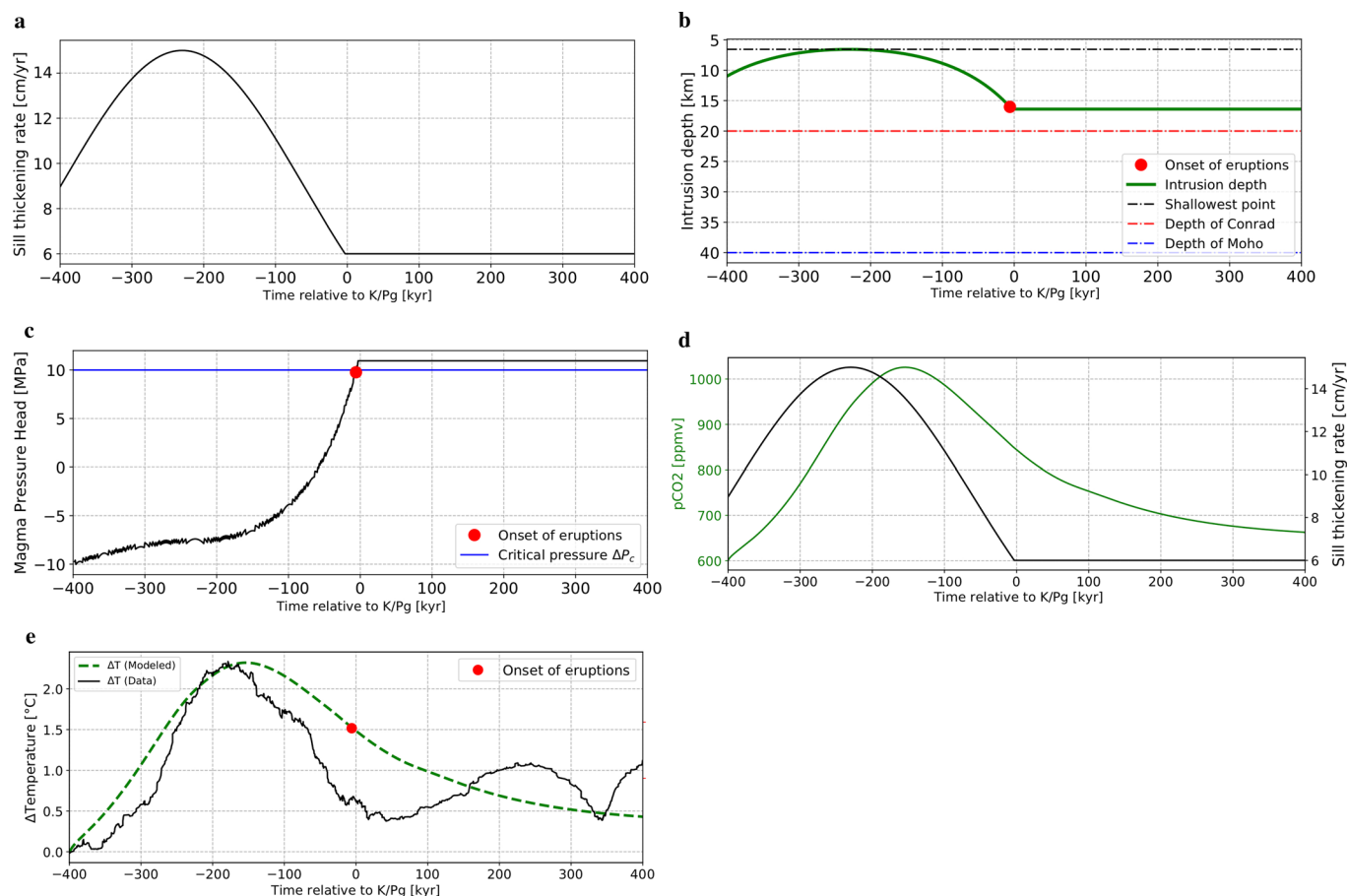
Extended Data Fig. 1 | Example of the steady-state analytic model results as functions of time relative to the Cretaceous-Paleogene (K/Pg) boundary.
a, Assumed Gaussian sill opening flux in terms of magma volume flux per unit area of the sill. **b**, Sill intrusion depth for the melt flux of **(a)** and the thermal energy balance of Eq. (6). **c**, Magma pressure head at the surface sourced from the intruding sill. Magma eruption is possible when this pressure equals to the critical pressure ΔP_c at around K/Pg. For this case, magma flux from -400 kyrs to 0 kyrs is intruded. **d**, global averaged atmospheric CO_2 concentration with time predicted by the LOSCAR climate model. **e**, global temperature change predicted by the LOSCAR model along with the extrusive flux with time to compare with the observation in Fig. 1a.
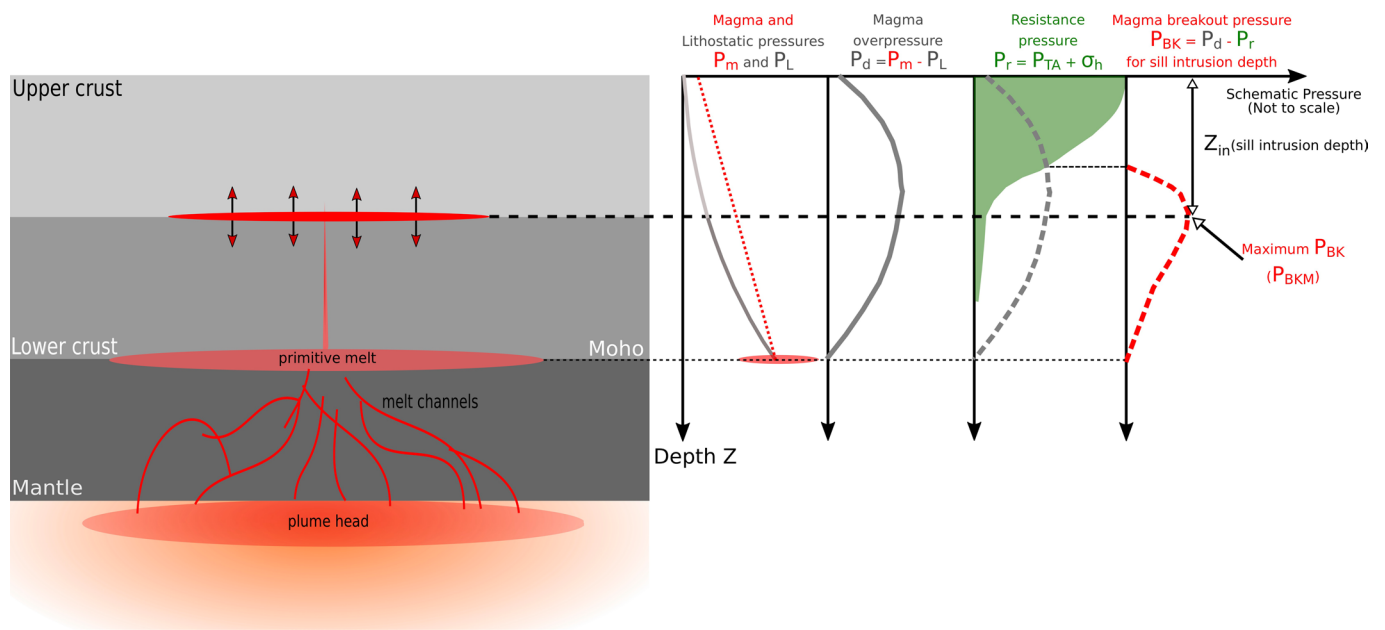
Extended Data Fig. 2 | Schematic illustrations of how to determine the depth for a sill intrusion at maximum breakout pressure. Magma overpressure (P_d), resistance pressure (P_r) and magma breakout pressure (P_{BK}) for determining sill intrusion depth (Z_{in}).